TOPICAL REVIEW

Klein tunneling in single and multiple barriers in graphene

To cite this article: J M Pereira Jr *et al* 2010 *Semicond. Sci. Technol.* **25** 033002

View the article online for updates and enhancements.

Related content

- Valley polarization due to trigonal warping on tunneling electrons in graphene
  J M Pereira Jr, F M Peeters, R N Costa Filho et al.

- Wavepacket scattering of Dirac and Schrodinger particles on potential and magneticbarriers
  Kh Yu Rakhimov, Andrey Chaves, G A Farias et al.

- Fractal spectrum of charge carriers in quasiperiodic graphene structures
  S H R Sena, J M Pereira Jr, G A Farias et al.

Recent citations

- Electronic confinement in graphene quantum rings due to substrate-induced mass radial kink
  L J P Xavier *et al*

- Partial pseudospin polarization, latticetronics and Fano resonances in quantum dots based in graphene ribbons: a conductance spectroscopy
  Luis I.A. López *et al*

- Magnetisation oscillations, boundary conditions and the Hofstadter butterfly in graphene flakes
  Yang Liu *et al*

TOPICAL REVIEW

Klein tunneling in single and multiple barriers in graphene

J M Pereira Jr[1], F M Peeters[1,2], A Chaves[1] and G A Farias[1]

[1] Departamento de Física, Universidade Federal do Ceará, Fortaleza, Ceará 60455-760, Brazil
[2] Department of Physics, University of Antwerp, Groenenborgerlaan 171, B-2020 Antwerpen, Belgium

Abstract
We review the transmission properties of carriers interacting with potential barriers in graphene. The tunneling of electrons and holes in quantum structures in graphene is found to display features that are in marked contrast with those of other systems. In particular, the interaction between the carriers with electrostatic potential barriers can be related to the propagation of electromagnetic waves in media with negative refraction indices, also known as metamaterials. This behavior becomes evident as one calculates the time evolution of wavepackets propagating across the barrier interface. In addition, we discuss the effect of trigonal warping on the tunneling through potential barriers.

(Some figures in this article are in colour only in the electronic version)

1. Introduction

The transmission of a particle through a classically forbidden region can be regarded as a quintessential quantum phenomenon, in the sense that it cannot be explained in the framework of Newtonian mechanics. The existence of such transmission, known as quantum tunneling, highlights the wave-particle duality that is at the core of the quantum picture of nature. The name of the phenomenon itself illustrates the counterintuitive aspect of the transmission, which takes place as if a particle, with some probability, could create a 'tunnel' which enables it to traverse a potential barrier that is higher than its energy. Although tunneling contradicts the expectations based on classical particle dynamics, it has a counterpart in optics, in the phenomenon of evanescent wave coupling, in which an electromagnetic wave is transmitted through a region where the solution of the corresponding wave equation is exponentially decaying. Likewise, the tunneling of a particle can be said to arise due to the coupling of the propagating solutions of Schroedinger's equation at either side of the potential barrier with decaying solutions in the barrier region, leading to non-zero transmission probability.

The concept of tunneling was first applied by Gamow [1] and, independently, by Condon and Gurney [2], in 1928 to explain nuclear alpha decay. In that case, the particle was a

helium nucleus and the potential barrier is provided by the confining nuclear potential. The success of that explanation soon led to the realization that tunneling is a general quantum phenomenon, and since then it has been observed in a variety of systems. Tunneling has also been exploited in the development of electronic devices, such as in the tunnel diode [3] and the resonant tunneling diode [4, 5].

Shortly after the introduction of quantum mechanics, several researchers started a search for a relativistic covariant version of the theory. That search culminated with the work of Dirac [6] in 1928, which presented an equation that provided a Lorentz-invariant description of the electron. That led to several important discoveries, such as the prediction of antimatter. One striking consequence of the theory was recognized by Klein [7]: for large potential steps, the Dirac equation generates results for tunneling that strongly contrast with the predictions of the non-relativistic theory. In particular, for a certain range of energies, the transmission probability for a single square barrier could reach 100%. The reason for this unusually high transmission is found in the overlap between positive and negative energy states outside and inside the barriers. That surprising result has been known as Klein tunneling [8].

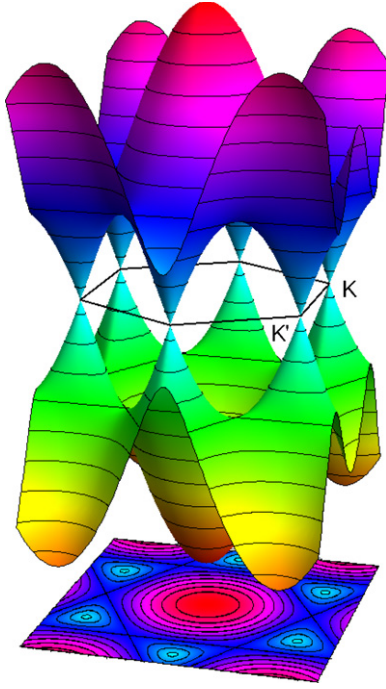Although there has been extensive experimental verification of the tunneling probability predictions of

Figure 1. Energy spectrum of graphene.

non-relativistic quantum mechanics, the detection of Klein tunneling has faced difficulties caused by the very large fields required for its observation. That situation has recently changed, as a consequence of an important development in solid state physics, a field that is apparently quite distant from the realm of relativistic quantum mechanics. That development was the fabrication of single layers of graphite, also known as graphene [9, 10], which in turn has spurred an extraordinary level of interest on the investigation of the properties of massless fermions (see e.g. [11] and [12]).

Graphene consists of single layers of graphite. It is a honeycomb lattice of covalent-bond carbon atoms, which can be treated as two interpenetrating triangular sublattices, labeled A and B, and can be pictured as unrolled, single-wall carbon nanotubes. An accurate microscopic description of the carrier dynamics of graphene is given by the tight-binding model. In this case, the free electron in each lattice site can hop to its neighboring sites. If one considers only nearest-neighbor hopping, the Hamiltonian can be written as

$$\mathcal{H} = \sum_{i,j} t_1 \left(a_i^\dagger b_j + b_j^\dagger a_i \right), \tag{1}$$

where $t_1 \approx 2.8$ eV is the nearest-neighbor hopping parameter and $a_m^\dagger$ (a_m) creates (destroys) an electron state at an m-labeled site in sublattice A, whereas the b and $b^\dagger$ operators do the same for sublattice B. The Hamiltonian (1) can be easily diagonalized to give [13]

$$E = \pm t_1 \sqrt{3 + f(\mathbf{k})}, \tag{2}$$

where

$$f(\mathbf{k}) = 2\cos\left(k_y a \sqrt{3}\right) + 4\cos\left(k_x 3a/2\right)\cos\left(k_y a \sqrt{3}/2\right), \tag{3}$$

with a the lattice parameter. This spectrum displays six cones with vertices that cross $E = 0$, of which only two are inequivalent, labeled K and K′ in figure 1. Their positions in

the reciprocal space are

$$\mathbf{K} = \left(\frac{2\pi}{3a}, \frac{2\pi}{3\sqrt{3}a} \right), \qquad \mathbf{K}' = \left(\frac{2\pi}{3a}, -\frac{2\pi}{3\sqrt{3}a} \right). \tag{4}$$

Thus, in the vicinity of **K** one can translate the momentum values as

$$k_x = k_x' - 2\pi/3a, \qquad k_y = k_y' - 2\pi/3\sqrt{3}a. \tag{5}$$

By expanding the structure factor for the hexagonal lattice in the vicinity of the cones, and by retaining the first-order terms, the Hamiltonian in the vicinity of **K** becomes

$$\mathcal{H} = \begin{pmatrix} 0 & \hbar v_F(k_x' - \mathrm{i}k_y') \\ v_F(k_x' + \mathrm{i}k_y') & 0 \end{pmatrix}, \tag{6}$$

where $\hbar v_F \equiv 3at_1/2$, and v_F gives the Fermi velocity of the electrons. The low-energy band structure of graphene is therefore gapless and the corresponding electronic states are found near the two cones located at inequivalent corners of the Brillouin zone. Thus, the low-energy carrier dynamics in the vicinity of the two cones is equivalent to that of a two-dimensional (2D) gas of massless charged fermions, which is governed by the Hamiltonian

$$\mathcal{H} = v_F(\sigma_x \tau_z p_x + \sigma_y p_y), \tag{7}$$

where $\hat{\mathbf{p}} = (p_x, p_y)$ is the momentum operator, v_F is the effective speed of light of the system, which in this case corresponds to $v_F \approx 1 \times 10^6$ m s^{-1}, and $\vec{\sigma}$ and $\vec{\tau}$ are Pauli matrices describing the probability amplitudes for the states at each sublattice (σ_z) and each inequivalent valley (τ_z), K and K′. In the absence of short range (i.e. of the order of a) potentials, the valley states are degenerate and the Hamiltonian can be written in the reduced form

$$\mathcal{H} = v_F(\vec{\sigma} \cdot \hat{\mathbf{p}}). \tag{8}$$

The Hamiltonian (7) acts on the states represented by the two-component spinors $\Psi = [\psi_A, \psi_B]^T$, where ψ_A and ψ_B represent the envelope functions associated with the probability amplitudes at the respective sublattice sites of the honeycomb graphene structure. The low-energy spectrum of free carriers is $E = \pm \hbar v_F (k_x^2 + k_y^2)^{1/2}$, with k_x and k_y the wavevectors along the x and y axes, in the vicinity of the cones at the Brillouin zone; the $+ (-)$ sign refers to electron (hole) bands. Equation (8) also implies that the carriers in each valley are chiral particles, with the projection of the pseudospin (σ_p) for electrons (holes) being aligned parallel (antiparallel) to the direction of propagation: $\sigma_p = (\vec{\sigma} \cdot \hat{\mathbf{p}})/|\mathbf{p}|$. Since it commutes with the Hamiltonian, the chirality of the carriers remains conserved even in the presence of an external electrostatic field. One way of breaking this conservation is by adding a mass term in the Hamiltonian (8), which can be written as $\mathcal{H}_m = m v_F^2 \sigma_z$, that couples the different components of the in-plane pseudospin, and in turn introduces a gap in the spectrum.
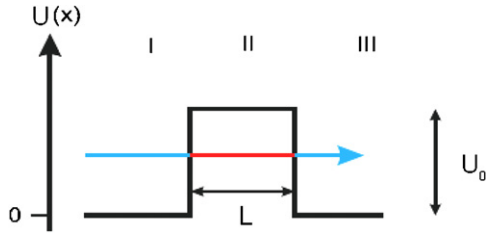
Figure 2. Schematic depiction of a square barrier with height U_0 and width L.

2. Klein tunneling in graphene

The absence of a gap in the spectrum, together with the conservation of chirality for carriers in graphene, leads directly to an important consequence: the suppression of backscattering by potential barriers. This unusual aspect of tunneling in this new material was first pointed out by Katsnelson *et al* [14], by calculating the tunneling coefficients for square barriers in single and bilayer graphene.

A potential barrier can be created in graphene by considering the effect of a gate voltage, which can be included in the Hamiltonian by adding a potential U. This leads to the equation

$$[v_F(\vec{\sigma} \cdot \hat{\mathbf{p}})]\Psi = (E - U)\Psi. \tag{9}$$

Let us consider a square barrier of width L along the x axis given by $U(x) = U_0(1 - \theta(|x| - L/2))$, $U_0 > 0$ (see figure 2). Although the potential barrier is abrupt, one can assume that the potential is smooth on the scale of the lattice parameter. It can be shown that for smooth potentials, the general behavior of the transmission is qualitatively similar to the present case. Since in this case the y component of the momentum operator commutes with the Hamiltonian, we can consider solutions in the form $\psi_C(x, y) = \phi_C(x)\,e^{ik_y y}$, $C = A, B$, and obtain

$$d\phi_B/d\xi + \beta\phi_B = i(\epsilon - u)\phi_A, \tag{10}$$

$$d\phi_A/d\xi - \beta\phi_A = i(\epsilon - u)\phi_B, \tag{11}$$

where $\xi = x/L$, $\beta = k_y L$, $\epsilon = E L/\hbar v_F$, $u = U(x) L/\hbar v_F$ are dimensionless.

The two coupled first-order differential equations, equations (9) and (10) can be transformed into a single second-order differential equation giving for ϕ_A the result

$$\frac{d^2\phi_A}{d\xi^2} + \frac{u'}{(\epsilon - u)}\frac{d\phi_A}{d\xi} - \left[\beta^2 + \beta\frac{u'}{(\epsilon - u)} - (\epsilon - u)^2\right]\phi_A = 0, \tag{12}$$

where u' is the derivative of the potential. For a square well, these derivatives are Dirac delta functions. We can consider the solutions in the regions outside and inside the barriers, where $u' = 0$. Let us consider the propagating solutions $\psi_A(x, y) = \phi_A(x)\,e^{ik_y y}$, with

$$\phi_A(x) = \begin{cases} e^{i\kappa\xi} + B_1\,e^{-i\kappa\xi} & \xi < -1/2, \\ A_2\,e^{i\alpha\xi} + B_2\,e^{-i\alpha\xi} & -1/2 \leqslant \xi \leqslant 1/2, \\ A_3\,e^{i\kappa\xi} & \xi > 1/2, \end{cases} \tag{13}$$
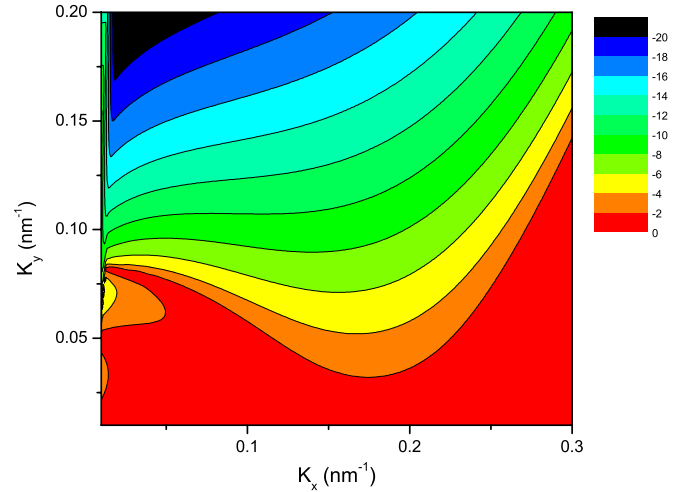

Figure 3. Contour plot of the electronic transmission through a single barrier with height $U_0 = 50$ meV and width $L = 50$ nm.

where $\kappa = [\epsilon^2 - \beta^2]^{1/2}$ and $\alpha = [(\epsilon - u_0)^2 - \beta^2]^{1/2}$. These solutions are similar to the ones obtained from Schroedinger's equation. However, the fact that in the present case the equations are of first order (which leads to the terms with the derivatives of the potential in the decoupled second-order equation) implies that the continuity of the derivatives of the spinor components at the barrier interfaces is not required. Thus, by matching the solutions at each region of constant potential, taking into account the continuity of ϕ_A and ϕ_B at the potential interfaces, one can obtain an explicit formula for the total transmission as $T = |A_3|^2$, where

$$A_3 = \frac{(g_+ - g_-)(f_+ - f_-)\,e^{-i\alpha}}{(g_+ - f_+)(g_- - f_-)\,e^{2i\kappa} - (g_+ - f_-)(g_- - f_+)}, \tag{14}$$

with $g_\pm = (\beta \pm i\kappa)/(\epsilon - u_0)$ and $f_\pm = (\beta \pm i\alpha)/\epsilon$.

A contour plot of the transmission as a function of the momentum components of the incident electron is shown in figure 3. For normal incidence (i.e. $k_y = 0$), the figure shows perfect transmission, characteristic of the Klein phenomenon. One important aspect of this result is the highly anisotropic character of the transmission in this system, with the appearance of several transmission peaks for non-perpendicular incidence. These resonance peaks are similar to Fabry–Pérot resonances in optical systems and can enhance the tunneling current for certain energies. This feature was investigated for smooth potential steps in single-layer graphene by Cheianov and Fal'ko [15]. These authors considered a smooth p–n junction and obtained, for incidence angles $\theta \ll \pi/2$, the transmission as a function of the angle for a potential step of width d as

$$T(\theta) = e^{-\pi(k_F d)\sin^2\theta}, \tag{15}$$

where k_F is the Fermi momentum of the carriers.

The fact that carriers in graphene can be reflected by potential steps for non-normal incidence implies that confined carrier states can be obtained, as long as they have a non-zero momentum component in the direction parallel to the barrier. Therefore, discrete energy levels may be found
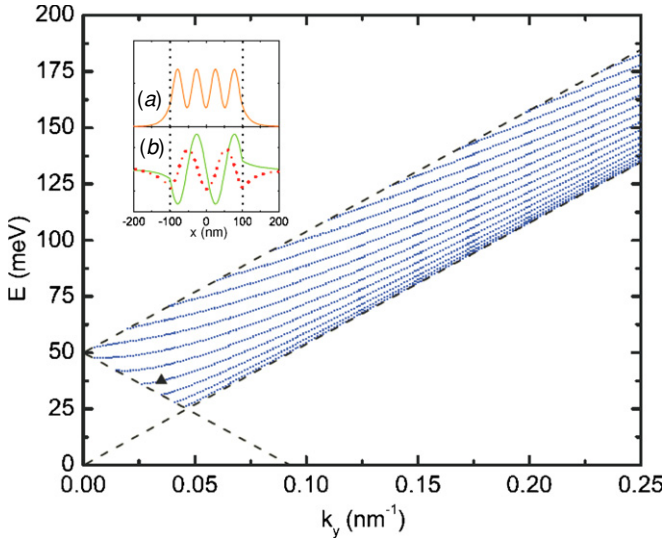
3

Figure 4. Spectrum of confined states in a graphene *square* QW versus k_y for $U_0 = 50$ meV and $L = 200$ nm. The lower inset shows (a) ϕ_A and $i\phi_B$ for the state shown by the solid triangle and (b) the related probability density.

for carriers in graphene-based quantum wires [16]. For a wire of width L defined by a square potential of the type $U(x) = U_0 \theta(|x| - L/2)$, $U_0 > 0$, the energy eigenvalues can be found by solving a transcendental equation. Requiring the continuity of ϕ_A and ϕ_B at $\xi = -1/2$ and $\xi = 1/2$, we obtain the following transcendental equation for the energy eigenvalues:

$$S_-(\epsilon, \beta, +1)S_+(\epsilon, \beta, +1) + S_-(\epsilon, \beta, -1)S_+(\epsilon, \beta, -1) = 0,$$
(16)

where $S_\pm(\epsilon, \beta, s) = \beta - f_\pm(\epsilon) - s\alpha\delta^{\mp s}$ and $\delta = \tan(\alpha/2)$. The results are shown in figure 4 for $U_0 = 50$ meV and $L = 200$ nm. The dashed lines delimit the continuum region, which corresponds to free electrons ($E \geqslant \hbar k_y + U_0$) with energies larger than the barrier height, and free holes ($E \leqslant -\hbar v_F k_y + U_0$) that propagate in the system by means of the Klein tunneling mechanism. The cut-off at low wavevectors thus arises due to the conversion of confined electrons to free holes. That is a consequence of the gapless spectrum of graphene, which allows the existence of unoccupied states in the valence band in the barrier region at the energies of the incident electrons even for small values of U_0. For large values of k_y, the dispersion branches are given approximately by $E = \hbar v_F \left[(n\pi/L)^2 + k_y^2 \right]^{1/2}$, where n is an integer. The lower inset (a) of figure 4 shows the two spinor components, for $k_y = 0.03$ nm^{-1}, shown by the solid triangle, whereas the upper inset (b) of figure 4 shows the corresponding probability density in arbitrary units. The vertical dotted lines indicate the position of the walls of the barrier. The spinor function plots clearly indicate a discontinuity in the derivative of the spinor component functions at the barrier interfaces, while the probability density is continuous.

The massless character of the carriers in graphene allows for an analogy between their propagation and the behavior of light in dielectric media. In this regard, it has been recognized

that the interaction of electrons and holes in graphene with p–n junctions is akin to that of light with media that display a *negative* refraction index, also known as *metamaterials*. This becomes evident if one calculates the deviation of an electron from the conduction band incident on a potential barrier with an angle θ_c. The transmitted portion of the wavefunction propagates in the barrier region with a 'refraction' angle θ_v, such that the relationship between these angles and the momenta is analogous to Snell's law of refraction:

$$\frac{\sin\theta_c}{\sin\theta_v} = -\frac{E}{|E - U_0|}.$$
(17)

Thus, the potential barrier can be interpreted as a region of negative refraction index $n = -k_v/k_c$ (as opposed to the 'vacuum' region outside the barrier, with $n = 1$).

That realization has led to the prediction by Cheianov *et al* that the flow of electrons in this system can be focused by means of n–p–n junctions [17], producing what is known as a Veselago lens [18]. The analogy between light propagation in dielectric media and the dynamics of carriers in graphene is particularly evident if one investigates the propagation of wavepackets in this system [19]. One particularly powerful technique for that study is the method of *split operators*.

3. Scattering of a wavepacket on a barrier

The propagation of wavepackets in ideal graphene has been recently studied, both numerically and analytically [20, 21], using a Green's function method which allowed the investigation of the oscillatory electronic motion (Zitterbewegung) that has been predicted from the relativistic analogy for the behavior of the electronic states in graphene. Below we show how the interaction of a Gaussian wavepacket with a potential barrier in graphene can be studied by a suitable application of the time evolution operator, using the split operator method. This technique has been successfully applied to investigate the properties of semiconductor structures [22] and can be readily extended to deal with carriers in graphene.

Let us first rewrite the Hamiltonian, including a mass term, which can be used to induce confinement or to mimic the effect of the edges of the graphene sheet,

$$\mathcal{H} = v_f \hbar(\sigma \cdot \mathbf{k}) + U(x, y)\mathbf{I} + F(x, y)\sigma_z,$$
(18)

where $U(x, y)$ is the potential, $F(x, y)$ is the mass term and $\mathbf{I}$ is the 2×2 unity matrix. In this method, the time evolution operator for carriers is written as a summation of two parts: one contains the potential and mass terms, which depend only on real space coordinates, whereas the other contains the momentum terms. Thus, the operator becomes

$$\exp\left[-\frac{i}{\hbar}H\Delta t\right] = \exp[-i\Xi_1]$$
$$\times \exp[-i\overrightarrow{\Xi}_2 \cdot \overrightarrow{\sigma}]\exp[-i\Xi_1] + O(\Delta t^3),$$
(19)

where $\Xi_1 = \frac{\Delta t}{2\hbar}[F(x, y)\sigma_z - U(x, y)\mathbf{I}]$ and $\overrightarrow{\Xi}_2 = \Delta t v_F \overrightarrow{k}$. The $O(\Delta t^3)$ error is a consequence of the fact that Ξ_1 and $\overrightarrow{\Xi}_2 \cdot \overrightarrow{\sigma}$ do not commute.

The exponentials can be expressed in terms of the matrices M_1 and M_2, written in the space of positions and momenta, respectively, as

$$M_1 = \begin{pmatrix} \exp\left[-i\frac{\Delta t}{2\hbar}(U+F)\right] & 0 \\ 0 & \exp\left[-i\frac{\Delta t}{2\hbar}(U-F)\right] \end{pmatrix} \quad (20)$$

and

$$M_2 = \cos(\Xi_2)\mathbf{I} - i\frac{\sin(\Xi_2)}{\Xi_2}\begin{pmatrix} 0 & \Xi_{2x} - i\Xi_{2y} \\ \Xi_{2x} + i\Xi_{2y} & 0 \end{pmatrix}, \quad (21)$$

where $\Xi_2 = \Delta t v_f \sqrt{k_x^2 + k_y^2}$ is the magnitude of the vector $\overrightarrow{\Xi}_2$.

Now we can obtain the wavefunction at a posterior time starting from an initial wavefunction as

$$|\Psi\rangle_{t+\Delta t} \simeq M_1 \cdot M_2 \cdot M_1 |\Psi\rangle_t, \quad (22)$$

where the terms of higher order in Δt are neglected, and where before (afterward) the multiplication of matrix M_2, we must perform a direct (inverse) Fourier transform on the function, in order to map it to the reciprocal (real) space. Note that if the Hamiltonian has neither external potentials nor mass terms, that is, $U(x,y) \equiv 0$ and $F(x,y) \equiv 0$, the separation between the real and reciprocal space-dependent terms in equation (19) is no longer necessary, and the multiplication of the initial wavefunction by the matrix M_2, defined by equation (21), gives the exact solution of the time evolution of the wavepacket for any value of Δt. However, in the case where $U(x,y)$ or $F(x,y)$ is non-zero, the $O(\Delta t^3)$ error induced by the non-commutativity of the terms of the Hamiltonian restricts the method to small values of Δt.

For the initial wavefunctions, we take Gaussian functions

$$\psi(x,y) = \frac{1}{\delta\sqrt{2\pi}} \exp\left[\frac{(x-x_0)^2}{2\delta_x^2} + \frac{(y-y_0)^2}{2\delta_y^2} + ik_x^i x\right], \quad (23)$$

where now we have two parameters δ_x and δ_y, to describe the width of the initial wavepacket in the x and y directions, respectively. For the sake of simplicity, we consider a wavepacket with circular symmetry, i.e. $\delta_x = \delta_y = \delta$. Thus, the initial spinor becomes

$$\Psi(x,y) = \begin{pmatrix} c_1 \\ c_2 \end{pmatrix} \psi(x,y), \quad (24)$$

where c_1 and c_2 define the initial pseudospin polarization.

Figure 5 shows the propagation of a wavepacket with width $\delta = 50$ nm as it interacts with a potential step $U = U_0\theta(y)$. The figure shows a contour plot of the probability density for four different instants. In this case, the incident angle is $\theta_i = \pi/4$, which is obtained using $c_1 = 1$ and $c_2 = \exp[i\pi/4]$, and $E = 100$ meV with $U_0 = 200$ meV. Thus, in agreement with the modified Snell's law, equation (13), the refraction angle obtained is $\theta_r = \pi/4$. The figure shows the probability density as a function of the position at four different moments, namely before the arrival of the wavepacket at the interface ($t = 0$ fs), the initial deformation of the wavepacket ($t = 140$ fs), the splitting of the wavepacket into refracted
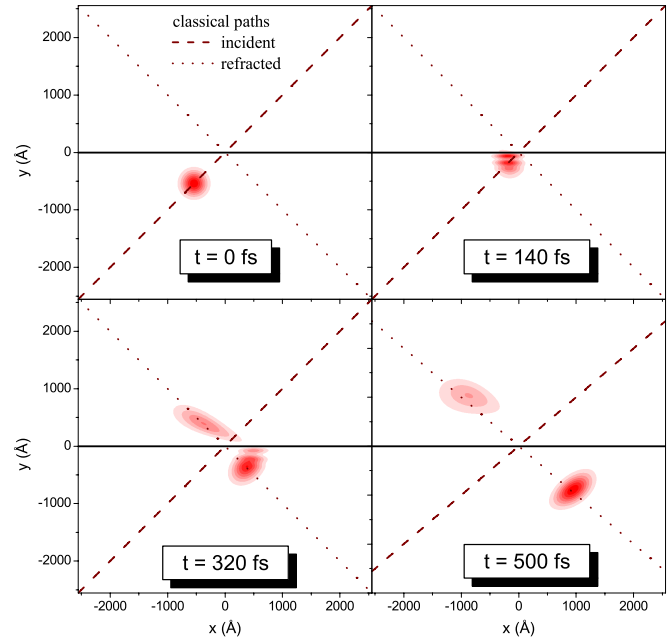
Figure 5. Time evolution of a wavepacket in graphene interacting with a potential step of height U_0, with $E = U_0/2$ and incidence angle $\theta_i = \pi/4$.

and reflected components ($t = 320$ fs) and the subsequent propagation of the two components ($t = 500$ fs). It is seen that both the reflected and refracted components are significantly deformed in comparison with the original circular-symmetric incident wavepacket. In this case, the existence of a reflected wavepacket is a direct consequence of the non-zero incident angle, which leads to a non-zero wavevector component in the direction parallel to the barrier. This, as shown in figure 3 for the single barrier, reduces the transmission coefficient of the potential step. Additionally, the results of figure 5 are in striking contrast with the usual non-relativistic picture, which does not allow for a transmitted wavepacket when the potential step has $E < U_0$.

The transmission of a wavepacket through a square potential barrier is shown in figure 6. In this case, the width of the barrier is $L = 50$ nm, and the other parameters are the same as in the previous figure. The dashed lines indicate the trajectory of the refracted wavepacket, as well as the path in the absence of a barrier. The dotted lines delimit the width of the barrier. As shown, the potential barrier causes a shift of the path of the transmitted wavepacket. This shift agrees with the result obtained from the analogy to the geometrical optics expressions, taking into account the negative refraction index associated with the barrier. For a wavepacket reaching a barrier of thickness L with an incident angle θ, a straightforward calculation, taking into account the refraction of the classical paths, gives a shift

$$d = L\frac{\sin(\theta_c + \theta_v)}{\cos\theta_v}. \quad (25)$$

Using equation (17) this result can be expressed as

$$d = L\sin\theta_c\left(1 + \frac{\cos\theta_c}{\sqrt{(k_v/k_c)^2 - \sin^2\theta_c}}\right). \quad (26)$$
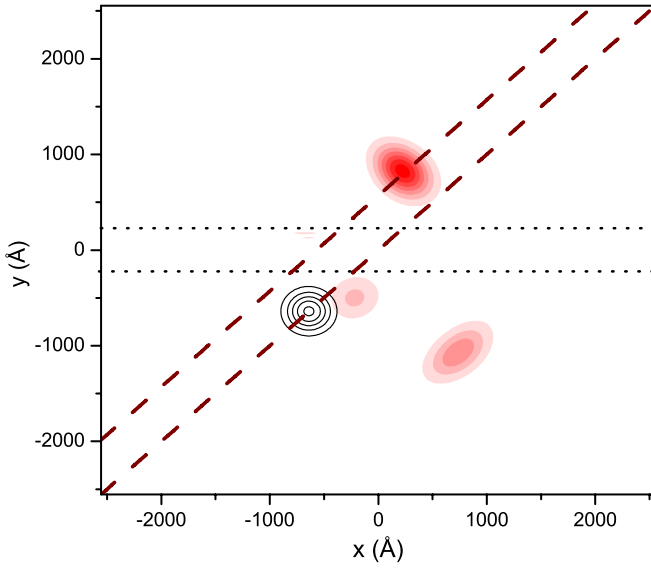
Figure 6. Time evolution of a wavepacket in graphene interacting with a potential barrier of height $U_0 = 200$ meV. The electron has average energy $E = 100$ meV and incidence angle $\theta_i = \pi/4$.

This shift is distinct from the one expected for a reflected wavepacket, known as the Goos–Hänchen effect, which has been recently investigated [23].

In the lower half of the graph some reflected components can be observed, which arise from the interaction of the wavepackets with each potential interface.

4. Multiple barriers

The lack of backscattering, the anistropy of the transmission of carriers in graphene, together with their long mean free path, suggest that resonance effects may be relevant to the properties of graphene-based quantum structures. This dependence becomes evident as one analyzes the conductance of multiple-barrier systems [24, 25]. For a single barrier, the total current for ballistic electrons presents oscillations as function of energy, due to an oscillation of the angular dependence of the transmission, caused by Fabry–Pérot-like resonances inside the barrier. The introduction of several barriers causes the appearance of additional resonance peaks in the transmission which, at low energies, causes additional oscillations of the total current. For multiple barriers, the energy spectrum of the carriers shows the appearance of minibands for non-normal propagation.

In order to simplify the discussion of the multiple-barrier case, let us rewrite the wavefunction for a region of constant one-dimensional potential $U(x) = U_i$ in the matrix form as

$$\Psi(x) = \mathcal{G}_i \mathcal{M}_i \begin{pmatrix} A_i \\ B_i \end{pmatrix} \qquad (27)$$

where

$$\mathcal{G} = \begin{pmatrix} 1 & 1 \\ g_-^i & g_+^i \end{pmatrix}, \qquad \mathcal{M} = \begin{pmatrix} e^{i\alpha_i x} & 0 \\ 0 & e^{-i\alpha_i x} \end{pmatrix}, \qquad (28)$$

and $g_\pm^i = (k_y \pm \alpha_i)/(\epsilon - u_0)$ and $\alpha_i = \sqrt{k_y^2 - (\epsilon - u_i)^2}$. If we apply the continuity condition for the wavefunction at
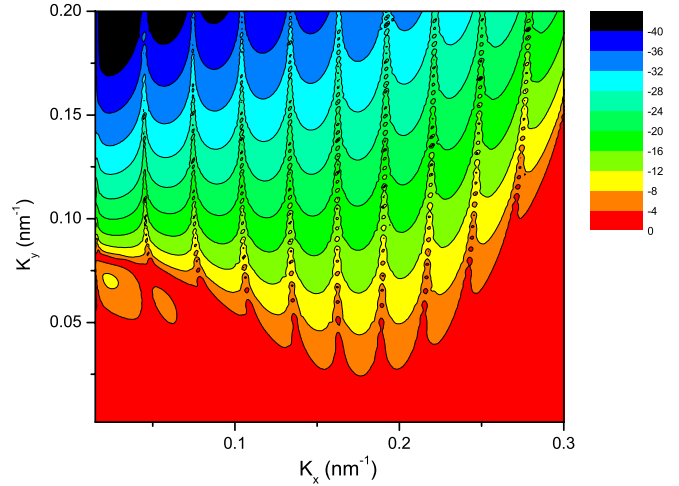

Figure 7. Contour plot of the logarithm of the transmission in wavevector space components for a double barrier with height $U_0 = 50$ meV, barrier width 50 nm and barrier separation $d = 100$ nm.

the interface of a potential step that separates two regions described by the potentials U_i and U_{i+1} at $x = x_i$, we can relate the amplitude coefficients at neighboring regions by

$$\begin{pmatrix} A_{i+1} \\ B_{i+1} \end{pmatrix} = \mathcal{N}_{i+1} \begin{pmatrix} A_i \\ B_i \end{pmatrix}, \qquad (29)$$

where $\mathcal{N}_{i+1} = \mathcal{G}_{i+1}^{-1} \mathcal{M}_{i+1}^{-1} \mathcal{G}_i \mathcal{M}_i$ is the transfer matrix that relates the wavefunction in regions i and $i + 1$. Thus, if one considers a set of $2m$ square barriers, the transmission coefficient can be calculated as

$$T = \frac{1}{|[\mathcal{N}]_{22}|^2}, \qquad (30)$$

where $[\mathcal{N}]_{22}$ is an element of the matrix given by the product

$$\mathcal{N} = \mathcal{N}_{2m} \mathcal{N}_{2m-1} \cdots \mathcal{N}_1. \qquad (31)$$

The dispersion relation is given by

$$2\cos(\kappa l) = \text{Tr}(\mathcal{N}), \qquad (32)$$

where $\kappa = 2\pi m/L$.

For a periodic potential profile, we have $\det[\mathbf{T}] = 1$. Assuming periodic boundary conditions we can write, for P unity cells, $\mathcal{N}^P = 1$. It follows that the eigenvalues of $\mathcal{N}$ are $e^{2\pi i m/P}$, with m an integer, and its determinant is equal to 1.

A (k_y, k_x) contour plot of the logarithm of the transmission T through a double barrier is shown in figure 7. In this case, each barrier has height $U_0 = 50$ meV and width $L = 50$ nm. The distance between the barriers is $d = 100$ nm. As seen, T depends on the direction of propagation or incident angle θ ($\tan\theta = k_y/k_x$) and displays a similar behavior as for the single-barrier case. The main difference between single and double barriers is an oscillatory increase of the transmission for all regions when a double barrier is considered. This results from an additional resonance effect, caused by the quasiconfined electron states between the barriers.

The first two minibands of the dispersion relation for a 1D graphene-based superlattice are plotted in figure 8. In this case,
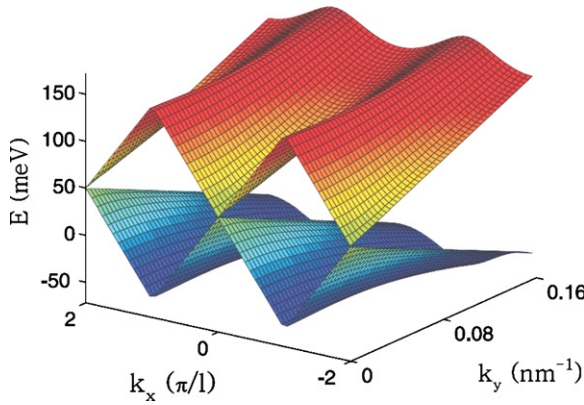
Figure 8. Dispersion relation in a 1D graphene SL with potential barriers of height $U_0 = 100$ meV, width 10 nm and separation $d = 10$ nm. Only the first two bands around the Dirac point are shown.
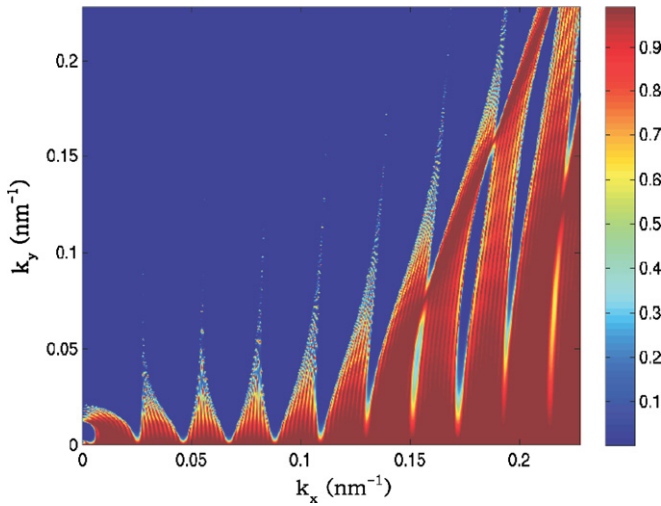

Figure 9. Contour plot of the transmission T of relativistic fermions in a structure consisting of ten units with $U_0 = 50$ meV, $L = 50$ nm and separation between barriers $d = 100$ nm.

the width of the wells and of the barriers is the same, and equal to 10 nm. Note that the form of the dispersion relation in the k_y direction, in contrast with the non-relativistic case, depends on the x component k_x of the wavevector. As a result, one cannot split the energy of the minibands as $E_n = E_n(k_x) + v_F \hbar k_y$. If k_y is sufficiently large, this dependence goes away and a linear relation between the energy and k_y is recovered, independently of the k_x component. Also, for $k_y = 0$ the linear dispersion relation $E(k_x, 0) = v_F \hbar k_x$ is unaltered by the periodic potential U, being only shifted by $U_0/2$.

Figure 9 shows a contour plot of the transmission for a multiple-barrier structure consisting of ten units. The main effect of having many units is a slight reduction in the continuous range of k_x for which perfect transmission occurs by the appearance of small gaps between regions of perfect transmission. This behavior remains essentially unaltered if the number of units is increased and is similar to that reported previously in the context of resonant tunneling through a double barrier [24].
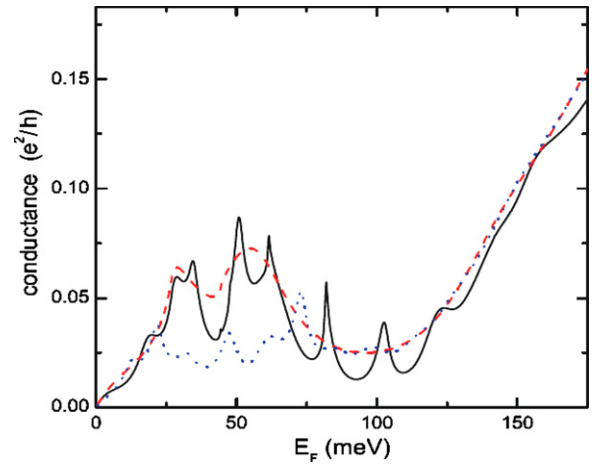

Figure 10. Conductance through single (dashed curve), symmetric (solid curve) and asymmetric (dotted curve) double barrier versus Fermi energy E for barriers with $L = 50$ nm. The height of the first barrier $U_0 = 100$ meV and that of the second $U_0 = 100$ and 50 meV. The inter-barrier separation is $d = 50$ nm.

5. Tunneling current

In an experimental setup, one usually measures the current J through the barrier. In the ballistic regime, the current is proportional to a weighted integral of the transmission $T(k_x, k_y)$. For the linear spectrum $E = \hbar v_F k$ the current J, due to a voltage drop eV along the x direction, is given by ($\lambda = 2ev_F/h^2$)

$$J = -\lambda \int T(E, \theta)[f(E) - f(E + eV)]E \, \mathrm{d}E \cos \theta \, \mathrm{d}\theta, \tag{33}$$

where $f(E)$ is the Fermi function. For low temperatures we can approximate $[f(E) - f(E + eV)]$ by $-eV\delta(E - E_F)$ and extract the low-bias conductance from equation (28).

Figure 10 shows the conductance versus the Fermi energy for a single barrier (dashed curve) and for a double symmetric (solid curve) and asymmetric (dotted curve) barrier, for barrier width $L = 50$ nm. The height of the first barrier is $U_0 = 100$ meV and that of the second is $U_0 = 100$ and 50 meV, for the solid and dotted curve, respectively. The inter-barrier separation is $d = 50$ nm. A pronounced resonant structure is found that is most explicit for symmetric barriers.

6. Trigonal warping effects

For an infinite, defect-free graphene sheet, the carrier states associated with each non-equivalent valley are degenerate. Nevertheless, there have been proposals to develop structures that can selectively act on these valley states, in order to create 'valleytronic' devices [26], in analogy with spintronic devices. Most of these proposals require the use of valley-selective interaction of carriers with the edges of graphene point contacts. Recently, there have been several works that investigated the effect of valley polarization on the tunneling through potential barriers [27, 28]. These studies focused on the effect of trigonal warping on the tunneling probability. Trigonal warping is a modification of the conical dispersion of

the carriers as the energy scale increases, due to the symmetry of the crystal lattice. The results show that the inclusion of trigonal warping introduces an anisotropy in the transmission that is valley dependent.

The energy of the carriers in single-layer graphene in the vicinity of the Dirac points can be obtained from a tight-binding model by expanding the energy equation (3) around the K and K' points. The effect of trigonal warping is manifested in the higher order momentum terms, which become increasingly significant in comparison with the linear term as the carrier energy increases away from the charge neutrality point and causes the spectrum to deviate from the conical shape, modifying the constant energy curves in the momentum space from circles to approximately triangular shapes (see figure 1).

Thus, by taking into account the leading higher order terms in the structure factor expansion, the carrier energy can be expressed in the presence of a potential U as

$$E = \pm \hbar v_F \sqrt{k^2(1 - 3sk_xa/2) + 2sk_x^3a + k^4a^2/16} + U, \quad (34)$$

where $s = 1(-1)$ for electrons in the K (K') valley and a is the distance between nearest-neighbor carbon atoms in graphene ($a \approx 0.142$ nm). The k_x (k_y) component of the momentum corresponds to propagation along the armchair (zigzag) direction in the lattice.

In this case, the calculation of the transmission coefficient is similar to the one described in the previous sections, except that due to the trigonal warping effect; the results for large potentials become sensitive not only to the direction of the electron momentum with respect to the potential barrier but also with respect to the lattice. One may consider two cases: square barriers in which the potential interface runs parallel to the zigzag side of the lattice and barriers with the potential interface along the armchair side.

In the zigzag case, the solutions inside and outside the barrier are matched along the zigzag direction of the lattice. The x-component of the wavevector (i.e. the component perpendicular to the barrier) is given by

$$k_x = \pm \left[-\frac{8}{a^2}\left(1 - \frac{3ask_y}{2}\right) - k_x^2 \right. $$
$$\left. \pm \frac{8}{a^2}\sqrt{\left(1 - \frac{3ask_y}{2}\right)^2 - \frac{k_y^3a^3s}{2} + \frac{a^2}{4}(\epsilon - u)^2} \right]^{1/2}.$$
$$(35)$$

This shows that trigonal warping creates an anisotropy of the dispersion, given that the value of k_x is sensitive to the sign of k_y. Therefore, this anisotropy should be present in the transmission properties of electrons through potential barriers. This anisotropy creates the asymmetry in the angular dependence of the transmission shown in figure 11. The figure shows the transmission coefficient for carriers with $E = 50$ meV, interacting with a square barrier of $U_0 = 200$ meV and $L = 500$ nm. The solid line shows the results for $s = 1$ (i.e. K valley), whereas the dashed line corresponds to $s = -1$ (K' valley). For lower barrier heights (e.g. $U_0 \lesssim 150$ meV), the asymmetry in the transmission becomes less evident, and the result for the conical dispersion is recovered.
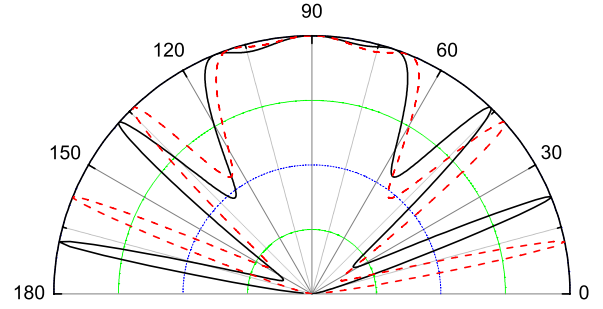

Figure 11. Incidence angle dependence of the transmission coefficient for a single barrier in the zigzag orientation, for carriers associated with K (solid black lines) and K' (red dashed) valleys. The potential barrier has height $U_0 = 200$ meV and width $L = 500$ nm, while the incident electron has energy $E = 50$ meV.
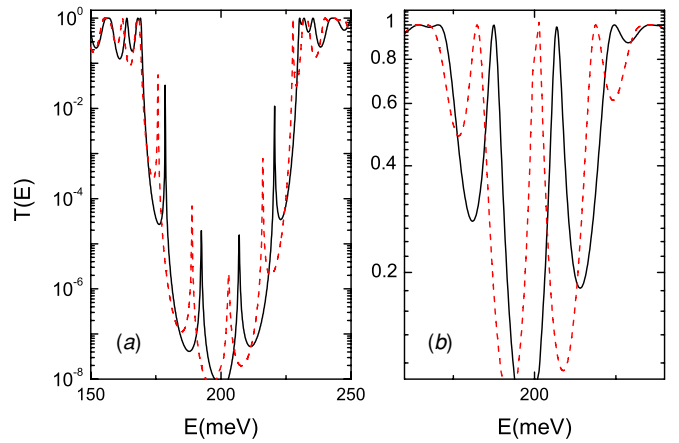

Figure 12. Transmission coefficient as a function of energy for a double barrier along the armchair orientation for carriers associated with K (solid black) and K' (dashed red) valleys for (a) $k_x = 0.05$ nm^{-1} and (b) $k_x = 0.01$ nm^{-1}.

For the armchair case, one has to find k_x by solving the equation

$$\frac{a^2}{16}k_x^4 + \left(\frac{as}{2}\right)k_x^3 + \left(1 + \frac{a^2}{8}k_y^2\right)k_x^2$$
$$- \left(\frac{3}{2}ask_y^2\right)k_x + \left[k_y^2 + \frac{a^2}{16}k_y^4 - (\epsilon - u)^2\right] = 0. \quad (36)$$

For a given energy, the values of k_x are expected to differ for different s. However, in contrast with the zigzag case, the transmission is expected to be invariant under a transformation of the momentum component parallel to the barrier, $k_y \rightarrow -k_y$. The asymmetry in the transmission in this case occurs between incoming electrons (i.e. moving 'to the right', with positive k_x) and outgoing (moving 'to the left', with negative k_x) electrons. The situation is reversed in each valley. Therefore, the large potential steps created in p–n junctions at an armchair orientation in graphene can create a valley-polarized current by means of a valley-selective transmission. Figure 12 shows results for a double barrier with $U_a = U_b = 200$ meV, $L_a = L_b = W = 100$ nm where (a) $k_y = 0.05$ nm^{-1} and (b) $k_y = 0.01$ nm^{-1}. The black solid line corresponds to incoming (outgoing) and the red dashed line to outgoing (incoming) carriers of the K (K') valley. As shown in [28], for the armchair case the total transmission

peaks of carriers through single and double barriers are shifted in energy depending on the valley label. This implies that the measured current as a function of the Fermi energy for potential barriers with $U_0 \gtrsim 200$ meV, which are within reach of current experiments, could show double peaks which can be explained by the valley polarization effect.

7. Conclusions

The production of graphene is expected to lead to a variety of device applications, ranging from transistors, transparent conducting films, to gas sensors. Nevertheless, on a more fundamental level the study of the properties of charge carriers in graphene has helped to shed light on new aspects of the phenomenon of quantum tunneling, and may allow the observation of several transmission effects that would be difficult to investigate in other 'classical' systems. The long mean free path of electrons and holes in graphene, together with the high quality of the samples being produced means that the observation of Klein tunneling, as well as resonance effects associated with tunneling become feasible, as shown by recent experimental studies [29, 30]. This can also be the case for other effects, such as electron focusing. Additionally, by modulating the valley polarization of the electron current by means of external gates, graphene may become the substrate of a new class of devices that exploit the valley degrees of freedom to perform logical operations.

Acknowledgments

References

[1] Gamow G 1928 *Z. Phys.* **51** 204
[2] Condon E U and Gurney R W 1928 *Nature (London)* **122** 439
[3] Esaki L 1958 *Phys. Rev.* **109** 603
[4] Tsu R and Esaki L 1973 *Appl. Phys. Lett.* **22** 562
[5] Sollner T C L G, Goodhue W D, Tannenwald P E, Parker C D and Peck D D 1983 *Appl. Phys. Lett.* **43** 588
[6] Dirac P A M 1928 *Proc. R. Soc. Lond.* **117** 610
[7] Klein O 1929 *Z. Phys.* **53** 157
[8] Dombey N and Calogeracos A 1999 *Phys. Rep.* **315** 41
[9] Novoselov K S, Geim A K, Morozov S V, Jiang D, Katsnelson M I, Grigorieva I V, Dubonos S V and Firsov A A 2005 *Nature (London)* **438** 197
[10] Zhang Y, Tan Y W, Stormer H L and Kim P 2005 *Nature (London)* **438** 201
[11] Geim A K and Novoselov K S 2007 *Nature Mater.* **6** 183
[12] Castro Neto A H, Guinea F, Peres N M R, Novoselov K S and Geim A 2009 *Rev. Mod. Phys.* **81** 109
[13] Wallace P R 1947 *Phys. Rev.* **71** 622
[14] Katsnelson M I, Novoselov K S and Geim A K 2006 *Nature Phys.* **2** 620
[15] Cheianov V V and Fal'ko V I 2006 *Phys. Rev.* B **74** 041403
[16] Pereira J M Jr, Mlinar V, Peeters F M and Vasilopoulos P 2006 *Phys. Rev.* B **74** 045424
[17] Cheianov V V, Fal'ko V and Altshuler B L 2007 *Science* **315** 1252
[18] Veselago V G 1968 *Sov. Phys. Usp.* **10** 509
[19] Sharma M and Ghosh S 2009 arXiv:0907.1631v2
[20] Maksimova G M, Demikhovskii V Ya and Frolova E V 2008 *Phys. Rev.* B **78** 235321
[21] Lherbier A, Biel B, Niquet Y-M and Roche S 2008 *Phys. Rev. Lett.* **100** 036803
[22] Degani M H and Leburton J P 1991 *Phys. Rev.* B **44** 10901
[23] Beenakker C W J, Sepkhanov R A, Akhmerov A R and Tworzydlo J 2009 *Phys. Rev. Lett.* **102** 146804
[24] Pereira J M Jr, Vasilopoulos P and Peeters F M 2007 *Appl. Phys. Lett.* **90** 132122
[25] Barbier Michaël, Peeters F M, Vasilopoulos P and Milton Pereira J Jr 2008 *Phys. Rev.* B **77** 115446
[26] Rycerz1 A, Tworzydlo J and Beenakker C W J 2007 *Nature Phys.* **3** 172
[27] Garcia-Pomar J L, Cortijo A and Nieto-Vesperinas M 2008 *Phys. Rev. Lett.* **100** 236801
[28] Pereira J M Jr, Peeters F M, Costa R N and Farias G A 2009 *J. Phys.: Condens. Matter* **21** 045301
[29] Stander N, Huard B and Goldhaber-Gordon D 2009 *Phys. Rev. Lett.* **102** 026807
[30] Velasco J Jr, Liu G, Bao W and Lau C N 2009 *New J. Phys.* **11** 095008